Monthly Notices of the Royal Astronomical Society
MNRAS **549**, 1–16 (2026)
Advance Access publication 2026 June 3
https://doi.org/10.1093/mnras/stag1005

High-precision *K2*/*TESS* photometry and HERMES spectroscopy of four bright field stars

Otto Trust,[1,2,3★] Santosh Joshi,[4] Benard Nsamba,[2,3,5] Sharon Aol,[1] Owen Vermeulen,[6] Ronald Ssembatya,[2] Peter De Cat,[7] Patricia Lampens,[7] Sydney A. Barnes,[8] Partha P. Goswami,[9] Athul Dileep,[4] Surath C. Ghosh,[4,10] Pramod S. Kumar,[11] Edward Jurua,[1] Mrinmoy Sarkar[4] and Sarabjeet S. Bedi[10]

[1]*Department of Physics, Mbarara University of Science and Technology, P.O. Box 1410, Mbarara, Uganda*
[2]*Department of Physics, Faculty of Science, Kyambogo University, P.O. Box 1, Kyambogo, Uganda*
[3]*Max-Planck-Institut für Sonnensystemforschung, Justus-von-Liebig-Weg 3, D-37077 Göttingen, Germany*
[4]*Aryabhatta Research Institute of Observational Sciences, Manora Peak, Nainital, Uttarakhand-263002, India*
[5]*Max-Planck-Institut für Astrophysik, Karl-Schwarzschild-Str. 1, D-85748 Garching, Germany*
[6]*Institute of Astronomy, KU Leuven, Celestijnenlaan 200D, B-3001 Leuven, Belgium*
[7]*Royal Observatory of Belgium, Ringlaan 3, B-1180 Brussel, Belgium*
[8]*Leibniz-Institutfür Astrophysik Potsdam (AIP), An der Sternwarte 16, D-14482 Potsdam, Germany*
[9]*Dakshin Kamrup College, Gauhati University, Guwahati, Assam-781125, India*
[10]*Department of CSIT, M. J. P. Rohilkhand University, Bareilly, Uttar Pradesh-243006, India*
[11]*Indian Institute of Astrophysics, Koramangala, Bangalore, Karnataka-560034, India*

Accepted 2026 May 22. Received 2026 May 22; in original form 2025 October 9

ABSTRACT

Space-based photometry from *K2* and *TESS*, coupled with high-resolution spectroscopy, provides a unique opportunity to re-examine the variability and chemical nature of four bright stars (HD 73135, BD +19° 2045, BD +19° 2046, and TYC 1395-855-1), which were poorly characterized by the original ground-based campaign under the Nainital–Cape survey. We aim to establish the nature of the variability, chemical properties, and evolutionary status of these stars. We analysed ground-based Johnson *BV* photometry combined with *K2* and *TESS* time-series data to establish the nature of their variability. Using high-resolution HERMES (High Efficiency and Resolution Mercator Echelle Spectrograph) spectroscopy, we determined their spectral classifications and chemical abundances. In addition, we used the inferred spectroscopic constraints with grid-based evolutionary modelling to derive their corresponding masses, radii, and ages. The frequency analysis reveals a diversity of low-amplitude variability across the sample. HD 73135 shows a persistent modulation near 1.5 d that is most consistent with rotation, although an ellipsoidal-binary interpretation cannot yet be excluded, while BD +19° 2045 exhibits multiple low-frequency signals and is identified as a new candidate γ Doradus *g*-mode pulsator. BD +19° 2046 and TYC 1395-855-1 are non-variable or only marginally variable in *K2* but display coherent low-frequency modulation in *TESS* of uncertain origin. Spectroscopically, HD 73135 is the only chemically peculiar star in the sample and shows a clear Am abundance pattern, whereas the other three stars are chemically normal. These results demonstrate the value of combining legacy survey data with contemporary photometric and spectroscopic analysis.

Key words: stars: chemically peculiar – stars: general – stars: rotation – starspots – individual: HD 73135, BD +19° 2045, BD +19° 2046, and TYC 1395-855-1.

1 INTRODUCTION

The Nainital–Cape (N–C) Survey was initiated in 1999 as a collaboration between the Aryabhatta Research Institute of Observational Sciences (ARIES), Nainital, India, and the South African Astronomical Observatory (SAAO), South Africa (B. N. Ashoka et al. 2000). The survey aimed at searching for and characterizing photometric variability, both pulsational and rotational, in candidate chemically peculiar (CP) stars, particularly of the Ap and Am types. Its main results were presented by P. Martinez et al. (2001) and extended by subsequent studies (e.g. S. Joshi et al. 2003, 2016), with most targets showing no significant pulsational variability.

The N–C survey focused primarily on CP stars, which are upper-main-sequence stars whose spectra display anomalous line strengths and surface abundances relative to normal stars of similar effective temperature (G. W. Preston 1974; G. Michaud, G.

★ E-mail: otrust@must.ac.ug

Alecian & J. Richer 2015). These peculiarities are understood to arise from processes such as atomic diffusion (including radiative levitation and gravitational settling) in relatively stable stellar atmospheres, and in many cases are linked to large-scale magnetic fields (G. Michaud et al. 2015). CP stars are of particular interest because surface abundance inhomogeneities can produce rotational modulation, and some subclasses (especially Am stars) can also exhibit low-amplitude pulsational variability (S. Turcotte et al. 2000; B. Smalley et al. 2017).

The N–C sample was assembled by selecting stars with Strömgren *uvbyβ* indices similar to those of known pulsating Ap and Am stars (S. Joshi et al. 2006, 2009). The adopted index ranges were chosen to isolate CP late-A to early-F stars, and were slightly broadened (by ∼10 per cent) to include somewhat cooler or more evolved objects (S. Joshi et al. 2006). The primary candidate list was drawn from Simbad photometric catalogues (B. Hauck & M. Mermilliod 1998), and supplemented by catalogues of Ap/Am stars (e.g. the Renson and Michigan compilations; see S. Joshi et al. 2009). However, the original survey did not include the high-resolution spectroscopy required for full chemical characterization of the targets, and this effort has therefore been pursued in subsequent phases (e.g. S. Joshi et al. 2017, 2022; A. Dileep et al. 2025; S. Joshi et al. 2025).

The variability of the N–C sample was established based on ground-based Johnson *BV* time-series photometry. However, ground-based photometric data suffer from diurnal sampling gaps and atmospheric systematics. Therefore, these data are mainly used to place conservative upper limits on the variability and to flag candidate periodicities for verification with space-based light curves.

The advent of long-baseline, high-precision photometry from space missions has transformed the study of stellar variability. The nominal *Kepler* mission, for example, revealed coherent low-amplitude signals at previously inaccessible precision (W. J. Borucki et al. 2010). The *K2* mission extended this capability to new sky fields (S. B. Howell et al. 2014; S. Joshi et al. 2022), and *TESS* has continued the legacy with its all-sky surveys (G. R. Ricker et al. 2015; G. Ricker 2021). Combined with high-resolution HERMES spectroscopy (G. Raskin et al. 2011) and forward-modelling methods (C. Aerts, J. Christensen-Dalsgaard & D. W. Kurtz 2010), such data now allow robust spectral classification, atmospheric parameter determination, and unambiguous interpretation of variability (rotation versus pulsation). This synergy enables a modern re-characterization of the N–C targets.

The N–C survey comprises 362 stars, none of which were observed during the nominal *Kepler* mission. However, *K2* data are available for twelve targets. Of these, five were classified as CP (Am) rotational variables by S. Joshi et al. (2022), while three stars (HD 23734, HD 68703, and HD 73345) were identified as chemically normal pulsating variables by S. Joshi et al. (2025). The remaining four stars, HD 73135, BD +19° 2045, BD +19° 2046, and TYC 1395-855-1, form the focus of the present study. For these objects, the availability of *K2* and *TESS* light curves, together with new HERMES spectroscopy, enables a level of characterization that was not possible at the time of the original survey.

Our observational strategy combines ground-based monitoring with *K2* and *TESS* photometry and new high-resolution HERMES spectroscopy. Using a uniform analysis of all four stars, we aim to (i) search for and characterize low-amplitude variability and assess the consistency of multiple photometric diagnostics, (ii) determine spectral classifications and atmospheric parameters and identify chemical peculiarities where present, and (iii) infer fundamental parameters, including mass, radius, and age, using MESA Isochrones and Stellar Tracks (MIST) evolutionary models (J. Choi et al. 2016; A. Dotter 2016). This study thus provides a consistent modern characterization of a set of previously poorly studied bright stars in the N–C survey sample, and connects legacy ground-based monitoring with contemporary space-based time-domain photometry.

The paper is structured as follows. Section 2 outlines the target selection, observations, and data reduction procedures. Photometric variability analysis is presented in Section 3, followed by spectral classification in Section 4. Section 5 describes the spectroscopic parameters and abundance determinations, while Section 6 discusses the fundamental parameters and evolutionary interpretation. Our conclusions and prospects are summarized in Section 7.

Table 1. Overview of *K2* campaigns (C05 and C18) and *TESS* sectors (S45 and S72) in which the programme stars were observed with the corresponding cadence.

Mission	*K2*	*K2*	*TESS*	*TESS*
Campaign/sector	C05	C18	S45	S72
Start date	27/04/15	12/05/18	06/11/21	11/11/23
End date	10/07/15	02/07/18	02/12/21	07/12/23
HD 73135	1800 s	1800 s	475 s	158 s
BD +19° 2045	1800 s 60 s	1800 s		158 s
BD +19° 2046	1800 s		475 s	158 s
TYC 1395-855-1	1800 s	1800 s		158 s

2 TARGET SAMPLE AND OBSERVATIONS

The four objects (HD 73135, BD +19° 2045, BD +19° 2046, and TYC 1395-855-1) define a quartet that was selected from the N–C survey sample to meet the following criteria: (i) availability of long- and/or short-cadence *K2* and *TESS* photometry (Table 1), (ii) comparable brightness ($V \simeq 8.6$–10.4 mag) to ensure uniform photometric precision, (iii) low line-of-sight extinction ($A_V <$ 0.15 mag), and (iv) closely matched ecliptic latitudes to minimize differential roll systematics and facilitate homogeneous reduction. The brightness of the targets ($V \simeq 8.6$–10.4 mag) makes them readily accessible to 1–2 m class telescopes.

The full data set therefore consists of (i) ground-based CCD photometry obtained with 0.4–1.3 m class telescopes, (ii) long-baseline *K2* and *TESS* space photometry, and (iii) high-resolution optical spectroscopy. The basic instrumental characteristics are summarized in Table 2, and a detailed observing log of the spectroscopic material is given in Table 3. Importantly, each star is observed in multiple independent data sets (ground-based, *K2*, and *TESS*) with different systematics. Comparing these data sets provides a robust check on signal persistence and supports a more conclusive interpretation of the variability.

2.1 Ground-based observations

Johnson *B* and *V* time-series of HD 73135 and BD +19° 2045 were obtained with the 1.04-m Sampurnanand Telescope at Nainital Observatory (ARIES; India), the 1.3-m Devasthal Fast Optical Telescope at Devasthal Observatory (ARIES; India), the 0.60-m Thai Southern Hemisphere Telescope (PROMPT-8) at Cerro

Table 2. Specifications of the telescopes and backend instruments used for the photometric and spectroscopic observations.

Category	Facility	Diameter (cm)	Location	Detector/spectrograph	FoV/resolution
Ground-based photometry	DFOT	130	Devasthal (India)	Andor DZ436	$18' \times 18'$
				Andor iXon EM+ DU-897	$4.7' \times 4.7'$
	ST	104	Nainital (India)	2k Wright CCD	$13' \times 13'$
	MASTER-II-URAL	40	Ural Federal University (Russia)	U16M CCD	$2^\circ \times 4^\circ$
	PROMPT-8	60	CTIO (Chile)	Apogee F42	$26.6' \times 22.6'$
Space-based photometry	*K2*	95	Space	–	$10.25^\circ \times 10.25^\circ$
	TESS	10.5 (per camera; 4 cameras)	Space	–	$24^\circ \times 96^\circ$
Spectroscopy	Mercator	120	La Palma (Canary Islands, Spain)	HERMES	$\mathcal{R} \simeq 85\,000$

Tololo Observatory (NARIT; Chile), and the 0.4-m MASTER-II-Ural telescope at Kourovka Observatory (Ural Federal University; Russia) (V. Lipunov et al. 2010; A. Y. Burdanov, V. V. Krushinsky & A. A. Popov 2014). Standard bias, dark, and twilight-flat frames were obtained on a nightly basis. The preliminary data reduction was performed using IRAF.[1] and it included bias/dark subtraction, flat-fielding, cosmic-ray cleaning, and aperture photometry with DAOPHOT (P. B. Stetson 1987). BD $+19^\circ$ 2046 and TYC 1395-855-1 were used as comparison stars for the differential photometry.

The light curves were analysed with Lomb–Scargle (LS) periodograms (N. R. Lomb 1976; J. D. Scargle 1982). The average amplitude of the residual spectrum after pre-whitening provides a proxy for the local noise. Following the commonly used criterion of M. Breger et al. (1993), we adopt SNR ≥ 4.0 as the significance threshold for independent frequencies; peaks with $3.5 \leq$ SNR < 4.0 are treated as tentative (M. Breger et al. 1999). Fig. 1 displays the resulting periodograms, where the dashed line marks the threshold SNR $= 4.0$.

Considering the tentative level ($3.5 \leq$ SNR < 4.0), peaks appear only in the *B*-band periodograms, with none in *V* reaching SNR ≥ 3.5. For HD 73135 (*B*), we find frequency peaks at $f \simeq 0.994$, 1.756, 2.997, and 7.046 d^{-1} (periods $\approx$ 1.006, 0.570, 0.334, and 0.142 d) with amplitudes $\approx$ 0.017–0.026 mag, while BD $+19^\circ$ 2045 (*B*) shows frequencies $f \simeq 0.954$ and 1.993 d^{-1} (periods $\approx$ 1.048 and 0.502 d) with larger amplitudes $\approx$ 0.10–0.12 mag. Peaks near ~ 1 and ~ 2 d^{-1} (and related harmonics, e.g. ~ 3 d^{-1}) are emblematic of diurnal window-function effects and differential extinction in ground-based data; their occurrence exclusively in *B* and absence in *V* therefore point to a non-astrophysical origin. For HD 73135, the peak at 7.046 d^{-1} lies in a δ Scuti-like frequency range but is borderline in significance and uncorroborated in *V*, and should be regarded as tentative. Overall, none of the peaks constitutes a secure stellar periodicity; a direct comparison with the space-based *K2* and *TESS* periodograms is presented in Section 3 (see also Tables 4–6).

2.2 *K2* space photometry

The *K2* data comprise Campaigns 5 and 18 for HD 73135, BD $+19^\circ$ 2045, and TYC 1395-855-1, while BD $+19^\circ$ 2046 is covered only in Campaign 5 (Table 1). In this paper, we describe the analysis of the long cadence data ($\sim$ 29.4-min) for all stars; however, a similar analysis was employed later for the short-cadence data ($\sim$ 58.8 s) available for BD$+19^\circ$ 2045. Long-cadence light curves were downloaded from MAST as Pre-search Data Conditioning Simple Aperture Photometry (PDCSAP) fluxes[2] For each campaign, we also obtained the K2 Systematics Correction (K2SC) products (S. Aigrain et al. 2015), which remove the dominant roll-angle drift trend.

Visual inspection showed that PDCSAP and K2SC curves agree within $\lesssim$300 ppm for all stars. Since K2SC occasionally introduces low-order trends in very quiet targets, we adopted PDCSAP fluxes as the default data set and used K2SC only as a consistency check. Fluxes were converted to relative units,

[1] IRAF is distributed by the National Optical Astronomy Observatory, which is operated by the Association of Universities for Research in Astronomy under a cooperative agreement with the National Science Foundation.
[2] https://archive.stsci.edu/k2/.

Table 3. The HERMES observation log for the target stars. The right ascension (α_{J2000}) and declination (δ_{J2000}) given by Gaia Collaboration (2021) and the *V*-band magnitude estimated by E. Høg et al. (2000) are included.

TIC no.	Other name	α_{J2000} (hh mm ss)	δ_{J2000} (dd mm ss)	V (mag)	BJD (2460 000+) (d)	Number of spectra	SNR (@ 500, 650, and 810 nm)	Total exposure duration (min)
195 192 995	HD 73135	08 37 18.2273	+18 52 11.8914	8.59	780	1	108, 113, 82	15
195 192 330	BD +19° 2045	08 36 29.8499	+18 57 57.0725	9.50	780	1	121, 113, 82	35
195 192 363	BD +19° 2046	08 36 34.5373	+18 51 13.2893	9.82	780	1	120, 59, 50	45
195 193 042	TYC 1395-855-1	08 37 01.6850	+19 01 38.6082	10.38	781	2	93, 73, 47	90

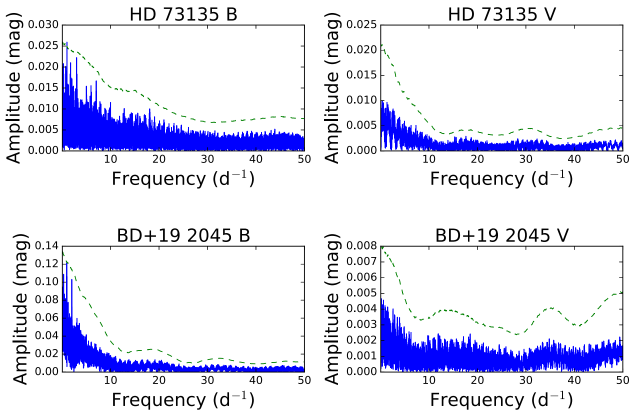

Figure 1. Lomb–Scargle periodograms of the ground-based Johnson *B* (left) and *V* (right) light curves. Top panels: HD 73135; bottom panels: BD +19° 2045. The ordinate is amplitude (magnitudes); the dashed line marks the SNR = 4.0 detection threshold, computed from a running-median noise estimate. Only the *B*-band spectra show peaks that reach the threshold, clustered near ∼1–2 d^{-1} (and harmonics) consistent with diurnal sampling/colour-dependent extinction; no significant periodicities are detected in *V*.

$\Delta F_i = F_i/\langle F\rangle - 1$, and the time series were shifted in such a way that $t(i) = t - t_0$, where t_0 was chosen as the time of the first observation in the corresponding light curve ($t_0 = 245\,7139.63$ d for C5 and 245 8251.55 d for C18).

The LS periodograms (Fig. 2) were computed up to the Nyquist frequency limit of 24.3 d^{-1}. A frequency peak was considered significant only if it appeared consistently in both observing campaigns (when available), in both the PDCSAP and K2SC light-curve extractions, and satisfied the false-alarm probability criterion FAP $\leq 10^{-8}$ (S. Joshi et al. 2022).

For each extracted frequency f_k, we define the phase as

$$\phi_k(t) = \mathrm{mod}[(t - t_0)\, f_k,\ 1]\,. \tag{1}$$

The phases reported in Tables 4 and 5 correspond to the fitted phase offsets of the sinusoidal model at the reference epoch t_0. Phase-folded light curves are computed using the same definition, adopting f_{dom} for the dominant periodicity shown in each panel.

The detected frequencies are listed in Tables 4 and 5. For all peaks above the adopted detection threshold, we applied iterative sinusoidal fitting and subtraction (pre-whitening), estimating formal uncertainties following M. H. Montgomery & D. Odonoghue (1999). Figs 2, A1, and A2 display the K2 light curves overlaid with the multi-frequency model fits, together with the corresponding LS periodograms and phase-folded light curves for the dominant periodicities. For visualization, phase-folded light curves are shown over two consecutive cycles ($0 \leq \phi < 2$).

2.3 *TESS* photometry

The *TESS* data span Sectors 44, 45, 46, and 72; however, Sectors 44 and 46 are strongly affected by instrumental artefacts for all targets, and Sector 45 is likewise affected for BD +19° 2045 and TYC 1395-855-1. We therefore exclude these affected sectors from our analysis. The combined baselines and cadences provide sensitivity to rotational modulation and low-frequency pulsations, if present.

We extracted aperture photometry from the *TESS* Full-Frame Images for the usable sectors listed in Section 2 and Table 1. The light curves were produced using a consistent extraction and cleaning procedure, as described below.

An optimal elliptical photometric aperture was determined for each target by minimizing the median absolute deviation of the resulting light curve, thereby maximizing the inclusion of target flux relative to background noise. Robust background subtraction was applied using a local annular background mask to estimate and remove the sky contribution. Outlier flux measurements were identified and removed through iterative sigma clipping.

All data processing was performed using the `lightkurve` package (Lightkurve Collaboration 2018) in conjunction with the `astropy` library (Astropy Collaboration 2013, 2018, 2022). Periodograms (see Fig. A3) were computed and significant periodic signals were identified following the methodology described in Section 2.2. The properties of the detected significant frequencies are summarized in Table 6.

2.3.1 *Time–frequency analysis toolkit*

All wavelet power spectra were computed using a custom python implementation of the Morlet wavelet transform (C. Torrence & G. P. Compo 1998), on a logarithmic grid of 200 scales spanning 0.5–80 d. We applied symmetric reflection padding to minimize edge effects and shade the cone of influence as defined in C. Torrence & G. P. Compo (1998). Global wavelet power spectra (GWPS) were obtained by summing the wavelet power over time at each scale and normalized to unit variance following Y. Liu, X. San Liang & R. H. Weisberg (2007). Autocorrelation functions (ACFs) were computed from linearly detrended *K2* and *TESS* light curves. The composite spectrum (CS) is defined as the geometric mean of the normalized GWPS and the ACF, following T. Ceillier et al. (2016, 2017), thereby emphasizing periodicities that are both strong and temporally persistent. The results are presented in Figs 3 and B1–B13.

Table 4. Sinusoidal components identified in the *K2* C5 light curves observed in 2015. Frequencies (f), periods (P), fractional-deviation semi-amplitudes (A), and phases (ϕ) were obtained by iterative pre-whitening (Section 2.2). Phases are given relative to the reference epoch t_0, chosen as the time of the first observation in each time-series data set. The final column gives $\log_{10}$(FAP), the base-10 logarithm of the false-alarm probability; more negative values denote more significant detections (our acceptance criterion is $\log_{10}$ FAP ≤ -8). One unit in A corresponds to 1086 mmag, and for each star the components are listed in order of decreasing A.

Star	f (d^{-1})	P (d)	$A(\times10^{-5})$	ϕ (rad)	$\log_{10}$ FAP
HD 73135					
	0.6973 ± 0.0005	1.434 ± 0.001	4.6 ± 0.3	-0.90 ± 0.07	-69
	0.6333 ± 0.0009	1.579 ± 0.003	2.4 ± 0.3	1.20 ± 0.18	-18
BD +19° 2045					
	0.1074 ± 0.0002	9.307 ± 0.020	64 ± 2	0.47 ± 0.02	-1000
	0.4257 ± 0.0004	2.349 ± 0.002	17.7 ± 0.9	-1.46 ± 0.05	-28
	0.1192 ± 0.0004	8.392 ± 0.028	13.8 ± 0.8	1.66 ± 0.06	-11
	0.0947 ± 0.0005	10.56 ± 0.05	12.1 ± 0.7	0.11 ± 0.06	-10
BD +19° 2046					
	0.0523 ± 0.0008	19.12 ± 0.29	6.8 ± 0.7	2.9 ± 0.1	-16
	0.1900 ± 0.0008	5.253 ± 0.024	6.7 ± 0.7	-0.9 ± 0.1	-14
TYC 1395-855-1	–	–	–	–	–

Table 5. Same as Table 4 but for *K2* Campaign 18 (2018).

Star	f (d^{-1})	P (d)	$A(\times10^{-5})$	ϕ (rad)	$\log_{10}$ FAP
HD 73135					
	0.651 ± 0.001	1.537 ± 0.003	2.9 ± 0.3	-3.10 ± 0.10	-22
	0.056 ± 0.001	17.8 ± 0.4	2.8 ± 0.3	-1.80 ± 0.10	-20
	3.860 ± 0.002	0.2591 ± 0.0001	1.7 ± 0.3	-2.7 ± 0.2	-11
	0.427 ± 0.002	2.34 ± 0.01	1.6 ± 0.3	-1.2 ± 0.2	-10
	0.499 ± 0.002	2.003 ± 0.007	1.6 ± 0.3	-1.3 ± 0.2	-9
BD +19° 2045					
	0.1151 ± 0.0004	8.687 ± 0.028	50 ± 2	1.53 ± 0.03	-221
	0.2215 ± 0.0004	4.515 ± 0.009	30 ± 2	-1.80 ± 0.04	-95
	0.3031 ± 0.0006	3.299 ± 0.006	17.3 ± 0.9	-0.96 ± 0.05	-34
	0.0796 ± 0.0007	12.56 ± 0.11	16 ± 1	2.29 ± 0.06	-22
	0.4050 ± 0.0006	2.469 ± 0.004	13.8 ± 0.8	1.69 ± 0.06	-21
	0.1009 ± 0.0008	9.91 ± 0.08	12.7 ± 0.9	0.04 ± 0.08	-16
	0.1264 ± 0.0008	7.91 ± 0.05	9.8 ± 0.7	-2.60 ± 0.08	-13
	0.3273 ± 0.0009	3.055 ± 0.008	8.2 ± 0.7	1.94 ± 0.08	-12
TYC 1395-855-1					
	0.100 ± 0.002	10.0 ± 0.2	4.1 ± 0.5	2.7 ± 0.2	-9

Table 6. Same as Table 4, but for *TESS* data. Frequencies (f), periods (P), fractional-deviation semi-amplitudes (A), phases (ϕ), and false-alarm probabilities are listed for the significant signals detected in the *TESS* light curves. Phases are given relative to the reference epoch t_0, chosen as the time of the first observation in each sector (see Section 2.2).

Star	Sector	f (d^{-1})	P (d)	$A(\times10^{-5})$	ϕ (rad)	$\log_{10}$ FAP
HD 73135	45	0.229 ± 0.002	4.37 ± 0.04	8.5 ± 0.70	2.457 ± 0.014	-17
	72	0.235 ± 0.002	4.26 ± 0.03	8.7 ± 0.60	1.366 ± 0.011	-36
		0.311 ± 0.002	3.21 ± 0.02	6.3 ± 0.60	0.485 ± 0.015	-14
BD+19° 2045	72	0.102 ± 0.001	9.83 ± 0.10	17.5 ± 0.80	1.829 ± 0.007	-101
		0.229 ± 0.001	4.38 ± 0.02	16.8 ± 0.70	2.2 ± 0.007	-92
		0.392 ± 0.001	2.55 ± 0.01	14.7 ± 0.70	2.352 ± 0.008	-68
		0.273 ± 0.002	3.66 ± 0.03	8.8 ± 0.70	0.064 ± 0.013	-18
		0.196 ± 0.002	5.10 ± 0.06	7.3 ± 0.70	0.812 ± 0.016	-9
BD+19° 2046	45	0.166 ± 0.002	6.04 ± 0.08	11.5 ± 1.1	0.462 ± 0.016	-11
	72	0.155 ± 0.002	6.40 ± 0.06	14.9 ± 1.0	1.057 ± 0.011	-33
TYC 1395-855-1	72	0.155 ± 0.001	6.47 ± 0.04	30.9 ± 1.2	0.61 ± 0.006	-124
		0.229 ± 0.001	4.37 ± 0.02	21.7 ± 1.2	1.075 ± 0.009	-56
		0.462 ± 0.002	2.17 ± 0.01	12.2 ± 1.2	1.821 ± 0.015	-11
		0.300 ± 0.002	3.34 ± 0.02	12.3 ± 1.2	1.509 ± 0.015	-11

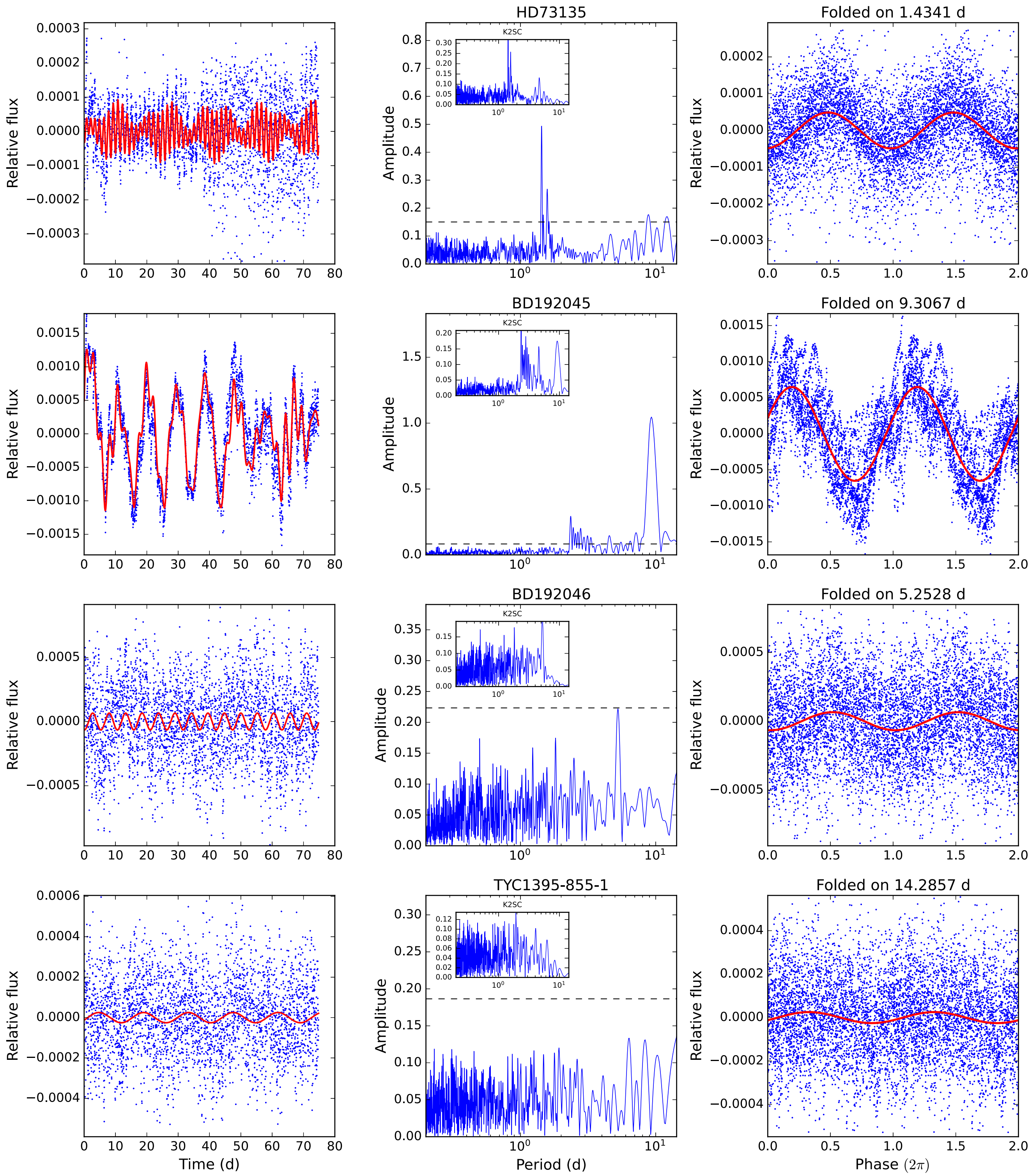

Figure 2. *Left panels:* Long cadence PDC light curves (*blue dots*) are overplotted with models including the significant frequencies (red line) for the four stars studied in this paper during the 2015 K2 Campaign 5. *Middle panel:* Lomb–Scargle periodograms. The period distribution (*blue*) has been plotted on a log-linear plot to aid visualization. An SNR of 4.0 is indicated by the black dashed horizontal line. The inset shows the Lomb–Scargle periodogram relating to the time-series after the application of the K2SC algorithm. *Right panel:* Campaign five time-series data (blue) phase-folded to the dominant period. The model for the dominant component (red) is produced from the data in Table 4.

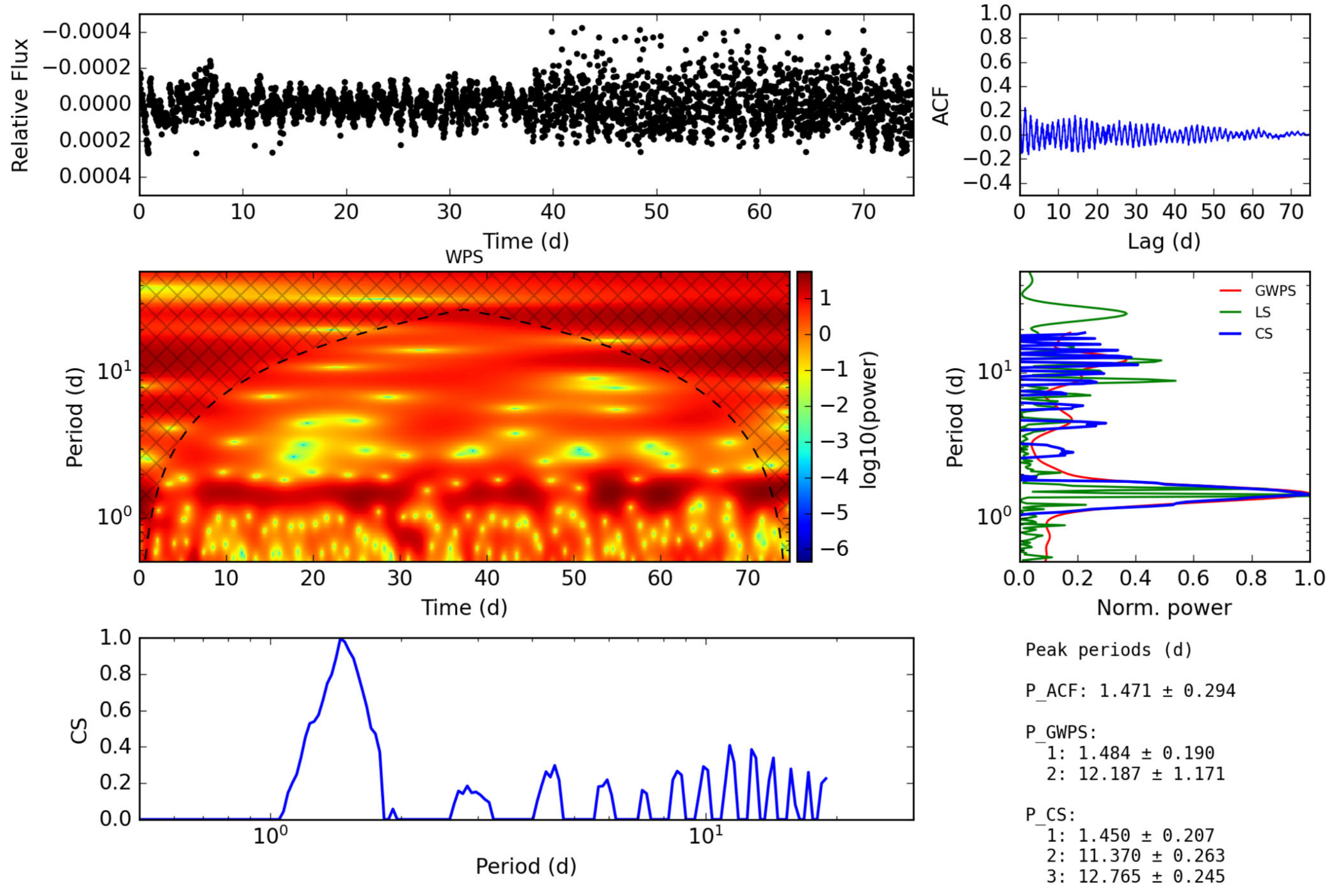

Figure 3. Period diagnostics for the *K2* C05 light curve of HD 73135. Top: light curve flux (left) and ACF (right). Middle-left: Morlet wavelet power spectrum ($\log_{10}$ power) computed on 200 logarithmically spaced periods spanning 0.5–30 d using symmetric reflection padding; the dashed curve marks the cone of influence (COI; C. Torrence & G. P. Compo 1998) and the hatched region indicates where edge effects become important. Middle-right: GWPS (red), Lomb–Scargle periodogram evaluated on the same period grid (LS; green), and their CS (blue), defined as the geometric mean of the normalized GWPS and ACF (T. Ceillier et al. 2016, 2017). Bottom-left: CS versus period. Bottom-right: dominant period from the first ACF peak (P_{ACF}) and the strongest peaks in GWPS and CS (P_{GWPS}, P_{CS}); uncertainties are estimated from peak half-height widths ($\sigma_P \simeq \mathrm{FWHM}/2.355$).

2.4 High-resolution spectroscopy

High-resolution spectra of all four stars were obtained with the HERMES échelle spectrograph (G. Raskin et al. 2011) equipped on the 1.2-m Mercator Telescope (La Palma) on 14–15 April 2025. In a single exposure, HERMES covers a wavelength range of 377–900 nm with spectral resolution of $\mathcal{R} \approx 85\,000$ and stability $\sim$50 m s^{-1}. The dedicated pipeline includes bias subtraction, flat-fielding, optimal order extraction, wavelength calibration using Th–Ar lamps, and blaze correction. Orders were merged and spectra were continuum normalized via low-order spline fits guided by templates from the Melchior library (P. Royer et al. 2024). Barycentric corrections were applied to each spectrum. Two exposures of TYC 1395-855-1 were median-combined, yielding SNR $\simeq$ 85 at 550 nm; single-exposure SNR values for the other stars range from 47 to 121. The resulting spectra form the basis for the spectral classification (see Section 4), atmospheric parameter, and abundance analyses (see Section 5).

3 NATURE OF VARIABILITY

Our four programme stars exhibit three qualitatively different kinds of variability in the space-based photometry. Because their precise evolutionary status is established only after the spectroscopic analysis and forward modelling described in Sections 5 and 6, we include a forward reference in parentheses at the first mention of each classification.

A direct comparison with the space photometry clarifies the status of the candidate peaks found in the ground-based data (Section 2.1). The dominant periodicities identified in the *K2* and *TESS* light curves for all target stars occur at much lower frequencies than the ground-based candidates: HD 73135 shows a stable signal at $f \simeq 0.63$–$0.70\,\mathrm{d}^{-1}$ ($P \simeq 1.4$–1.6 d) in *K2* Campaigns 5 and 18 (Tables 4 and 5), while BD +19° 2045 is dominated by $f \simeq 0.10$–$0.12\,\mathrm{d}^{-1}$ ($P \simeq 9$–10 d) in both *K2* and *TESS* (Tables 4–6). None of the prominent ground-based peaks near $\sim$1 and $\sim$2 d^{-1} is recovered as a dominant, persistent signal in the space-based periodograms, consistent with their interpretation as sampling/extinction artefacts.

A frequency is regarded significant only if the LS peak satisfies $\log_{10}(\mathrm{FAP}) \leq -8$ (approximately a $\sim 4\sigma$ detection) following S. Joshi et al. (2022). Because space-based periodograms evaluate a very large number of trial frequencies and may retain low-level instrumental systematics, we adopt this conservative threshold to define significant peaks. This criterion is intentionally more stringent than the ground-based amplitude signal-to-noise ratio (SNR) thresholds (Section 2.1), which are tailored to shorter, window-function-limited time series and are used there mainly to flag candidate peaks. Moreover, no single diagnostic is sufficient for low-frequency variability: the LS periodogram alone can be sensitive to residual systematics and harmonics, while real signals due to rotation or pulsation may vary in amplitude and phase with time. We therefore require *consistency* among four complementary diagnostics:

(i) the LS/pre-whitened frequency list (Tables 4 and 5);
(ii) the wavelet power spectrum (WPS → GWPS), which distinguishes spot-like rotational modulation (a single drifting ridge) from pulsational behaviour (multiple quasi-stationary ridges);
(iii) the ACF, whose first secondary maximum yields an independent rotational period, $P_{\rm ACF}$;
(iv) the CS, defined as the geometric mean of GWPS and ACF (T. Ceillier et al. 2016, 2017), which enhances periodicities that are both strong and time-persistent.

We classify the variability as *rotational* if (a) $P_{\rm LS}$, $P_{\rm ACF}$, $P_{\rm GWPS}$, and $P_{\rm CS}$ agree within their uncertainties; (b) the photometric period is compatible with the spectroscopic constraint $P_{\rm phot} \le P_{\rm max} \equiv 2\pi R/(v \sin i)$, where R is taken from Section 6; and (c) the WPS ridge broadens with time in a manner typical of spot evolution and/or differential rotation. We deem the variability of *pulsational* origin if multiple harmonically unrelated peaks cluster in the γ Doradus domain (0.3–3 d^{-1}), form narrow, quasi-stationary ridges in the WPS, and do not produce a coherent ACF signature.

3.1 Star-by-star classification from *K2* and *TESS* photometry

In *K2* Campaigns 5 and 18, HD 73135 shows a persistent low-frequency doublet at $f \simeq 0.63$–$0.70\,{\rm d}^{-1}$ ($P \simeq 1.4$–1.6 d) with highly significant detections (down to $\log_{10}$ FAP $\simeq -69$). The agreement between the LS, ACF, GWPS, and CS diagnostics, together with the broadening of the WPS ridge, supports rotational modulation by evolving surface inhomogeneities (e.g. abundance spots) and/or differential rotation. Using the radius from Section 6 and the measured $v \sin i$ (Table 10), we obtain $P_{\rm max} = 2\pi R/(v \sin i) \approx 1.8$ d, confirming that the $\sim$1.5 d modulation is compatible with rotation for a moderate inclination. In *TESS* (Sectors 45 and 72) the dominant low-frequency power shifts to longer time-scales ($P \simeq 3.2$–4.4 d; Table 6), which exceed $P_{\rm max}$ and therefore cannot represent the fundamental rotational period. We adopt the K2 $\sim$1.5 d signal as the rotational time-scale. Photometry alone cannot strictly exclude an orbital interpretation (ellipsoidal variability in a non-eclipsing binary), for which the dominant photometric signal typically occurs at $2f_{\rm orb}$; a dedicated radial-velocity time series is required to rule out this possibility.

BD +19° 2045 shows the most complex low-frequency variability in both *K2* and *TESS*. In *K2* C5, it is dominated by $f \simeq 0.108\,{\rm d}^{-1}$ ($P \simeq 9.30$ d), with additional significant peaks spanning ~ 0.09–$0.43\,{\rm d}^{-1}$; *K2* C18 and *TESS* Sector 72 show a rich but comparable pattern across ~ 0.08–$0.41\,{\rm d}^{-1}$, producing a quasi-stationary multi-ridge WPS morphology. Although the strongest periods are of order 9–10 d, the presence of multiple harmonically unrelated peaks and persistent, narrow ridges is consistent with γ Doradus g-modes rather than spot modulation. Crucially, a rotational origin is excluded by the spectroscopic constraint: the radius from Section 6 and $v \sin i$ (Table 10) imply $P_{\rm max} \approx 5.7$ d, which is incompatible with the observed $\sim$9–10 d periodicity. We therefore classify BD +19° 2045 as a new candidate γ Doradus g-mode pulsator.

In *K2* C5 data, BD +19° 2046 exhibits only low-significance power ($\log_{10}$ FAP ≥ -16) with semi-amplitudes $\lesssim 0.07$ mmag and no reinforcing ACF/CS signature, consistent with granulation (T. Kallinger et al. 2014) and/or residual *K2* roll-angle systematics (S. Aigrain, H. Parviainen & B. J. S. Pope 2016). In *TESS* (Sectors 45 and 72), the star shows a coherent modulation near $P \simeq 6.0$–6.4 d with agreement across the photometric diagnostics (Table 7). Given the small $v \sin i$ (Table 10), rotational period $P \simeq 6$ d would require a near pole-on inclination.

TYC 1395−855−1 is not detected as variable in *K2* C5 and shows only weak, marginal signals in *K2* C18 ($\log_{10}$ FAP $= -9$; Table 5), with intermittent WPS power and no coherent ACF signature. In contrast, *TESS* Sector 72 reveals clear low-frequency variability, including significant power near $P \simeq 6.4$ d and additional components at $P \simeq 2.2$–4.4 d (Table 6), with concordant photometric diagnostics. For TYC 1395−855−1, the small $v \sin i$ (Table 10) implies that a rotational interpretation would require a near pole-on geometry.

The discrepancy between the weak or absent *K2* variability and the coherent *TESS* signals in BD +19° 2046 and TYC 1395−855−1 is significant. Since *TESS* has a much larger pixel scale (G. R. Ricker et al. 2015) than *K2* (J. E. Van Cleve & D. A. Caldwell 2016), the extracted *TESS* light curves are more susceptible to flux contamination from nearby unresolved or partially blended sources. Therefore, although the *TESS* signals are coherent and appear significant in the photometric diagnostics, we cannot exclude the possibility that some or all of the detected low-frequency variability originates from contaminating stars within the *TESS* aperture rather than from the target stars themselves. We consequently classify the *TESS* detections in BD +19° 2046 and TYC 1395−855−1 as low-frequency variability of uncertain origin, pending confirmation from higher-spatial-resolution photometry or time-series spectroscopy.

In summary (see Table 7), the variability of HD 73135 is best explained by rotational modulation (supported by the $v \sin i$–R constraint in *K2*) but ellipsoidal variability remains a viable alternative without radial-velocity constraints, BD +19° 2045 is a robust new γ Doradus pulsator (rotation ruled out by $P_{\rm max}$), and BD +19° 2046 and TYC 1395−855−1 are non-variable or only marginally variable in *K2* but display coherent low-frequency signals in *TESS*, which we conservatively classify as uncertain pending additional constraints.

4 SPECTRAL CLASSIFICATION

Our primary goal is to establish temperature and luminosity anchors for the detailed abundance and forward modelling routine that follows (Sections 5 and 6). We adopted the Morgan–Keenan (MK) framework, which gives a uniform grid of spectral and luminosity types against which chemical peculiarities can be gauged (W. W. Morgan, P. C. Keenan & E. Kellman 1943; R. O. Gray & C. Corbally 2009).

Spectra were classified with the automated MKCLASS code (R. O. Gray & C. J. Corbally 2014). The programme implements the MK 'metric-distance' technique (J. LaSala 1994): each continuum-normalized target spectrum is degraded to the resolution of the reference library ($\mathcal{R} \simeq 2500$), rebinned to the 380–462 nm range, and compared to standard stars through a weighted least-squares metric. Separate metric-distance

Table 7. Summary of variability diagnostics. Columns (3–7): dominant significant period from the composite spectrum ($P_{\rm CS}$), semi-amplitude of the strongest LS peak ($A_{\rm max}$; 1 unit in A corresponds to 1086 mmag), range of $\log_{10}$(FAP), a concordance flag, and the variability classification. Concordance flag: 'Y' = all four metrics agree; 'N' = at least one metric disagrees or $\log_{10}$ FAP > -8.

Star	K2 campaign(s)/sector(s)	Dominant $P_{\rm CS}$ (d)	$A_{\rm max}$ (mmag)	$\log_{10}$ FAP range	Concordance	Classification
HD 73135	5, 18	1.45±0.21; 1.55±0.26	0.05	−69 to −9	Y	Rotation (surface inhomogeneities)
BD +19° 2045	5, 18	9.45±1.18; 8.82±1.07	0.70	−1000 to −10	Y	γ Doradus g-modes
BD +19° 2046	5	5.06±0.17	< 0.07	−16 to −5	N	Non-significant
TYC 1395−855−1	5, 18	18.06±0.33; 10.1±0.50	< 0.04	−9 to −4	N	Non-significant
HD 73135	45, 72	4.51±0.39; 3.49±0.55	0.09	−36 to −14	N	Long-period signal (inconsistent with $v \sin i$)
BD +19° 2045	72	9.9±0.68	0.20	−101 to −9	Y	γ Doradus g-modes
BD +19° 2046	45, 72	4.11±0.05; 6.38±0.29	< 0.16	−33 to −11	Y	Low-frequency variability (uncertain)
TYC 1395−855−1	72	7.33±1.22	< 0.34	−124 to −11	Y	Low-frequency variability (uncertain)

Table 8. Spectral classifications (typical uncertainty: ±1 subclass, ±0.5 luminosity class). A single MK type is quoted when k/h/m diagnostics agree; otherwise the k/h/m types are reported.

Star	This work	Literature
HD 73135	kA7 hF1 mF2 (Am)	A2 (1), Am (2)
BD +19° 2045	F8 V	F6 V (3)
BD +19° 2046	K1 IV–V, CN1	K0 (4)
TYC 1395-855-1	K2 IV, CN2	–

Note. **References:** (1) A. J. Cannon & E. C. Pickering (1993); (2) A. P. Cowley & C. R. Cowley (1965); (3) W. P. Bidelman (1956); (4) S. Roeser & U. Bastian (1988)

(least-squares mismatch) values are computed for the Ca II K line (k-type), the Balmer lines (h-type), and the metal-line region (m-type). If the k-, h-, and m-type classifications are consistent within the adopted uncertainty, we quote a single summary MK type. Otherwise we report the k/h/m types explicitly, since their mismatch is physically informative (e.g. for Am stars). Our standards are sourced from the Gray–Miller CCD library (R. O. Gray et al. 2003); additional plate-scanned spectra from A. P. Cowley & C. R. Cowley (1965) and S. Roeser & U. Bastian (1988) were used as tie-ins for the late-K range.

Monte Carlo tests with injected noise show that MKCLASS recovers the correct spectral sub-type within ±1 subclass and the luminosity class to ±0.5 class for spectra with SNR > 75, comparable to our HERMES data. Systematic errors may arise from rotational broadening ($v \sin i \gtrsim 70\,{\rm km\,s^{-1}}$) which weakens metallic blends and can bias the m-type to earlier classes; imperfect continuum placement when degrading HERMES $\mathcal{R} \sim 85\,000$ spectra to $\mathcal{R} = 2500$; the limited blue–violet coverage of the standard library, precluding the use of Ca I 4226 Å blend often used to separate K IV from K III.

Accordingly, we quote all the final classifications with a conservative '±1 subclass, ±0.5 luminosity class' uncertainty. CN-strength suffixes (CN1, CN2) are tentative because they rely on relative band-depths in spectra whose pseudo-continuum may still retain low-order blaze residuals.

Table 8 summarizes the classifications. HD 73135 → kA7 hF1 mF2: the five-subclass k-metal discrepancy identifies a classical Am star, consistent with the rotational modulation found in Section 3. BD +19° 2045 → F8 V (±1): consistent with the photographic F6 V classification of W. P. Bidelman (1956) within the typical ∼1–2 subtype uncertainty expected for photographic/low-resolution spectral classifications (mean rms ≃ 1.7 subtypes; T. Hippel et al. 1994); metal lines appear normal. BD +19° 2046 → K1 IV-V, CN1: the CN enhancement is mild (1σ detection) and will be revisited in the abundance analysis. TYC 1395-855-1 → K2 IV, CN2: strong CN bands suggest dredge-up of CNO-processed material, again to be checked in Section 5.

These spectral types provide the backbone for the atmospheric-parameter and evolutionary modelling that follow in Sections 5 and 6.

5 ASTROPHYSICAL PARAMETERS AND CHEMICAL ABUNDANCES

In order to obtain a self-consistent set of atmospheric parameters, we combined three complementary techniques, intermediate-band photometry, broad-band spectral-energy-distribution (SED) fitting, and high-resolution synthetic-spectrum fitting. Photometry and SED fitting provide initial estimates of stellar parameters, which are then refined through spectroscopic analysis and subsequently used to determine individual chemical abundances. The steps needed to estimate basic physical parameters, as well as the main uncertainties, are summarized here.

5.1 Photometry

Strömgren $uvby\beta$ indices were chosen because the combination of their m_1 and c_1 indices clearly separate effective temperature, surface gravity, and metallicity for A–G stars (T. T. Moon & M. M. Dworetsky 1985). We adopted the T. T. Moon & M. M. Dworetsky (1985) calibrations to derive photometric values of $T_{\rm eff}$, $\log g$, and [M/H]. The uncertainties quoted for the $uvby\beta$-based parameters listed in Table 9 (i.e. ± 200 K in $T_{\rm eff}$, ± 0.10 dex in $\log g$, and ± 0.13 dex in [M/H]) are adopted errors that incorporate measurement uncertainties, reddening uncertainties, and calibration scatter. The reddening $E(\rm B-V)$ was estimated from the 3-D dust map of G. M. Green (2018) and G. M. Green et al. (2019).

Near-infrared 2MASS (Two Micron All Sky Survey) colours anchor the Rayleigh–Jeans tail and help break the reddening–temperature degeneracy. The 2MASS JHK_s photometry was taken from the 2MASS All-Sky Point Source Catalog (R. M. Cutri et al. 2003). We used the catalogue magnitudes and uncertainties to form near-IR colours (e.g. $J-K_s$), which were dereddened using the adopted $E(\rm B-V)$ and a standard extinction law (e.g. G. H. Rieke & M. J. Lebofsky 1985; J. A. Cardelli, G. C. Clayton & J. S. Mathis 1989). Effective temperatures were then estimated from $(J-K_s)_0$ using the InfraRed Flux Method (IRFM) colour–$T_{\rm eff}$ calibration of J. I. González Hernández & P. Bonifacio (2009). Since the 2MASS-based temperatures are used only as initial guesses for the spectroscopic analysis, we assume solar metallicity in the calibration. The quoted 2MASS-based $T_{\rm eff}$ uncertainties listed in Table 9 include propagated photometric and reddening errors together with the intrinsic scatter of the calibration.

5.2 Effective temperature and log g from SED fitting

SEDs were built with VOSA (A. Bayo et al. 2008) using photometric measurements extracted from the Tycho-2, 2MASS, *WISE*, *Gaia* DR3, and (when available) GALEX, SDSS, and APASS data bases. Kurucz ATLAS9 ODFNEW/NOVER models were fitted via χ^2 minimization, using *Gaia* parallaxes as distance priors and $A_V = 3.1\,E(B-V)$ extinction. We fixed the model metallicity to solar composition ([M/H]= 0.0) in the SED fitting (e.g. G. Catanzaro et al. 2018; G. Catanzaro et al. 2019). Formal VOSA errors underestimate true systematics, so we follow the technique described by O. Trust et al. (2021) and adopt $\sigma_{T_{\rm eff}} = 250$ K, $\sigma_{\log g} = 0.25$ dex.

5.3 Radial velocity

Absolute velocities were measured with the Fourier cross-correlation algorithm of J. Tonry & M. Davis (1979) as implemented in ISPEC (S. Blanco-Cuaresma et al. 2014; S. Blanco-Cuaresma 2019). To ensure line-list consistency, we used synthetic templates computed at the $T_{\rm eff}$ and $\log g$ obtained from our photometry and SED analyses (Sections 5.1 and 5.2). A solar metallicity was assumed because $v_{\rm rad}$ is insensitive to modest abundance errors. The results are presented in Table 10. Statistical errors come from the Tonry–Davis $R_{\rm TD}$ value; a systematic ± 0.2 km s^{-1} floor (barycentric correction and instrumental drift) is added quadratically.

5.4 Projected rotational velocity

Projected rotational velocity ($v \sin i$) was derived entirely from synthetic-profile fitting. For each star, we generated a local ATLAS9 synthetic spectrum (the initial guesses of $T_{\rm eff}$ and $\log g$, solar abundances, and $v_{\rm rad}$ as in Section 5.3), convolved it with a rotational broadening kernel and performed a least-squares optimization with the MINUIT engine inside GIRFIT (Y. Frémat et al. 2006). The fit was repeated for contiguous 10 nm windows across 500–600 nm, a region rich in moderately strong metal lines but largely free of Balmer-wings and telluric contamination. The Mg I triplet was excluded for BD +19° 2046 and TYC 1395-855-1 because its strong damping wings bias the velocity kernel. The $v \sin i$ grid spanned 0–200 km s^{-1} in 1 km s^{-1} steps; the segment-to-segment scatter is adopted as the total uncertainty. The final values are listed in Table 10.

5.5 $T_{\rm eff}$ and log g from spectroscopy

We determined the atmospheric parameters by χ^2–minimization between normalized observed spectra and synthetic calculations. The latter were computed with the SPECTRUM radiative–transfer code, using atomic data from VALD, solar abundances from M. Asplund et al. (2009), and plane–parallel LTE ATLAS9 model atmospheres (F. Castelli & R. L. Kurucz 2003).[3] The workflow was implemented with ISPEC (S. Blanco-Cuaresma et al. 2014; S. Blanco-Cuaresma 2019).

For the hotter stars (HD 73135 and BD +19° 2045), we used the Hβ wings to refine $T_{\rm eff}$; and we did not use them to constrain $\log g$ (B. Smalley 2005). Surface gravities were instead determined from fitting the Fe I/Fe II lines and we selected only the lines that are unblended at the HERMES resolution and have a well-defined local continuum. For the cooler stars (BD +19° 2046 and TYC 1395−855−1), where Balmer profiles are weak and more susceptible to systematic effects, $T_{\rm eff}$ and $\log g$ were determined entirely from fitting Fe I/Fe II lines using the same line-selection criteria.

Parameter uncertainties combine the internal errors from the covariance matrix of the fit with systematic terms. Continuum normalization is a leading source of systematics in high-resolution work due to noise correlations (e.g. rebinning), line crowding, and the need to model broad spectral regions (e.g. R. Napiwotzki, D. Schoenberner & V. Wenske 1993; T. Morel & K. Butler 2006). We estimate the continuum-placement error as

$$\epsilon_{\rm cont} \simeq \frac{1.5}{\rm SNR}, \qquad (2)$$

with SNR measured per pixel (D. F. Gray 2005). To propagate this term, the observed spectrum was renormalized by factors $(1 \pm \epsilon_{\rm cont})$ and the fit repeated; the deviations from the nominal solution were adopted as the continuum-related uncertainties. To account for residual systematics not captured by the internal fit errors and the continuum-renormalization tests, we impose conservative minimum (floor) uncertainties of 150 K in $T_{\rm eff}$ and 0.15 dex in $\log g$ (D. Huber et al. 2014; I. U. Roederer & E. N. Kirby 2014), added in quadrature. The uncertainties reported in

[3] http://www.stsci.edu/hst/observatory/crds/castelli_kurucz_atlas.html.

Table 9. Basic parameters of the sample. Right ascension and declination (J2000) are from *Gaia* DR3 (Gaia Collaboration 2021).

Star	α (J2000)	δ (J2000)	E(B − V)	T_{eff} *uvbyβ*	log *g* *uvbyβ*	[M/H] *uvbyβ*	T_{eff} 2MASS	T_{eff} SED	log *g* SED
ID	(hh mm ss)	(dd mm ss)	(mag)	(±200 K)	(±0.10 dex)	±0.13	(K)	(±250 K)	(±0.25 dex)
HD 73135	08 37 18.2273	+18 52 11.8914	0.010 ± 0.002	–	–	–	7360±250	7250	4.0
BD +19°2045	08 36 29.8499	+18 57 57.0725	0.011 ± 0.002	6580	4.10	0.15	6480±220	6250	4.0
BD +19°2046	08 36 34.5373	+18 51 13.2893	0.026 ± 0.005	–	–	–	4770±190	4750	3.0
TYC 1395-855-1	08 37 01.6850	+19 01 38.6082	0.032 ± 0.006	–	–	–	5040±210	4750	3.25

Table 10. The fundamental astrophysical parameters as computed from high-resolution spectroscopy and the $\log(L_\star/L_\odot)$ as calculated from the *Gaia* DR3 parallaxes are listed. Quoted uncertainties include internal fit errors, continuum-renormalization tests, and adopted systematic floors added in quadrature (Section 5.5).

Star ID	T_{eff} (K)	log *g* (dex)	$[\mathrm{M/H}]_{\mathrm{model}}$ (dex)	[Fe/H] (dex)	ξ (km s^{-1})	$v \sin i$ (km s^{-1})	V_{rad}
HD 73135	7210 ± 190	3.95 ± 0.17	-0.47 ± 0.08	-0.08 ± 0.06	3.48 ± 0.34	66.0 ± 2.8	10.22 ± 1.46
BD +19° 2045	6440 ± 230	4.05 ± 0.20	-0.09 ± 0.11	$+0.04 \pm 0.06$	2.05 ± 0.25	17.0 ± 2.2	38.10 ± 0.22
BD +19° 2046	5270 ± 190	3.45 ± 0.23	-0.13 ± 0.06	-0.08 ± 0.05	1.37 ± 0.23	6.0 ± 2.8	45.65 ± 0.20
TYC 1395-855-1	5000 ± 210	3.13 ± 0.27	-0.04 ± 0.05	$+0.04 \pm 0.05$	1.10 ± 0.21	5.0 ± 2.2	13.78 ± 0.20

Table 11. Individual chemical abundances inferred for HD 73135, BD +19° 2045, BD +19° 2046, and TYC 1395-855-1. The solar abundances are listed in the last column (M. Asplund et al. 2009). The values are expressed in the form $\log(N_{\mathrm{el}}/N_{\mathrm{Tot}})$. The number of segments from which each element was determined is given in brackets.

Element	HD 73135	BD +19° 2045	BD +19° 2046	TYC 1395-855-1	Solar values
C	-4.16 ± 0.15 (11)	–	-3.50 ± 0.26 (11)	-3.62 ± 0.13 (3)	−3.57
O	-3.05 ± 0.23 (2)	−2.82 (1)	–	–	−3.31
Na	-5.36 ± 0.10 (3)	-5.47 ± 0.33 (4)	-5.58 ± 0.05 (3)	-5.28 ± 0.10 (7)	−5.76
Mg	-4.43 ± 0.11 (12)	-4.39 ± 0.13 (7)	-4.27 ± 0.16 (13)	-4.23 ± 0.12 (10)	−4.4
Al	-5.28 ± 0.08 (4)	–	-5.51 ± 0.09 (6)	-5.23 ± 0.17 (2)	−5.55
Si	-4.39 ± 0.09 (18)	-4.49 ± 0.13 (14)	-4.71 ± 0.14 (12)	-4.89 ± 0.18 (5)	−4.49
S	-4.58 ± 0.14 (7)	–	–	–	−4.88
K	−7.20 (1)	−6.42 (1)	–	–	−6.97
Ca	-6.12 ± 0.07 (19)	-5.46 ± 0.15 (17)	-5.60 ± 0.07 (26)	-5.42 ± 0.08 (19)	−5.66
Sc	-9.23 ± 0.19 (11)	-8.75 ± 0.09 (9)	-8.77 ± 0.07 (17)	-8.68 ± 0.09 (12)	−8.85
Ti	-7.08 ± 0.07 (28)	-7.03 ± 0.06 (22)	-6.86 ± 0.03 (32)	-6.83 ± 0.04 (27)	−7.05
V	–	−7.80 (1)	-7.61 ± 0.06 (17)	-7.56 ± 0.06 (17)	−8.07
Cr	-6.22 ± 0.10 (20)	-6.27 ± 0.07 (13)	-6.32 ± 0.05 (23)	-6.20 ± 0.04 (20)	−6.36
Mn	-6.66 ± 0.18 (4)	-6.52 ± 0.13 (6)	-6.24 ± 0.08 (16)	-5.97 ± 0.12 (15)	−6.57
Fe	-4.58 ± 0.04 (51)	-4.46 ± 0.04 (41)	-4.58 ± 0.02 (37)	-4.46 ± 0.02 (33)	−4.5
Co	−6.18 (1)	-7.22 ± 0.15 (2)	-6.99 ± 0.04 (23)	-6.97 ± 0.05 (17)	−7.01
Ni	-5.44 ± 0.04 (33)	-5.76 ± 0.08 (20)	-5.79 ± 0.02 (27)	-5.65 ± 0.04 (27)	−5.78
Cu	–	–	-7.10 ± 0.14 (2)	-6.47 ± 0.33 (3)	−7.81
Zn	-7.16 ± 0.43 (4)	-8.01 ± 0.36 (2)	-7.89 ± 0.02 (2)	–	−7.44
Ga	–	–	−9.15 (1)	–	−8.96
Sr	–	-8.99 ± 0.10 (3)	-9.19 ± 0.27 (3)	−9.73 (1)	−9.13
Y	-8.84 ± 0.18 (8)	-9.87 ± 0.17 (8)	-9.84 ± 0.08 (9)	-9.81 ± 0.31 (5)	−9.79
Zr	–	–	–	−9.57 (1)	−9.42
Ba	-8.71 ± 0.09 (6)	-9.70 ± 0.05 (6)	-9.51 ± 0.07 (6)	-9.71 ± 0.05 (7)	−9.82

Table 10 reflect the quadrature sum of the internal errors, the continuum-related terms, and these adopted floors.

Overall, the photometric, SED, and spectroscopic parameter estimates are broadly consistent (Tables 9 and 10). For HD 73135, the 2MASS-, SED-, and spectroscopic temperatures agree within ∼150 K; BD +19° 2045 likewise shows good consistency, with the spectroscopic solution lying between the photometric and SED estimates. TYC 1395−855−1 also shows satisfactory agreement within the adopted uncertainties. The largest discrepancy is found for BD +19° 2046, for which the spectroscopic solution is hotter and yields a somewhat higher log *g* than the photometric/SED estimates. In the analyses that follow, we adopt the spectroscopic parameters as the final values, while the photometric and SED determinations are treated as independent checks and initial constraints.

5.6 Microturbulent velocity

The microturbulent velocity (ξ) was determined within the global synthetic-spectrum fit. We constrained ξ by fitting the profiles of selected clean, moderately strong lines, requiring the synthetic spectra to reproduce the relative core and wing strengths. Fe I lines provided the primary constraint, while Ti II lines were included only as additional clean features to improve the stability of the fit. We retained only lines that are unblended at the HERMES resolution and have reliable VALD3 atomic data ($\log gf$ uncertainties ≤ 0.05 dex).

Uncertainties in ξ were estimated from the covariance matrix of the fit and verified with Monte Carlo noise tests; they scale approximately with 1/SNR and the inverse square root of the number of fitted lines. The resulting 1σ uncertainties are typically 0.21–0.34 $\mathrm{km\,s^{-1}}$. The final values are listed in Table 10. As shown in Fig. 4 , the synthetic spectra based on the atmospheric parameter values fit the observed spectra quite well.

5.7 Individual chemical abundances

The chemical abundance analysis was carried out using the spectroscopically determined fundamental parameters as input. Each stellar spectrum was partitioned into several local fitting windows, typically spanning 5–10 nm (50–100 Å), to enable reliable local continuum placement and line-profile fitting. These windows were selected manually, centred on diagnostically useful lines, and chosen to avoid severe blends, continuum defects, and telluric contamination. Within each window, elemental abundances were derived through a least-squares minimization procedure (W. H. Press et al. 2007).

We used the SYNTHV_NLTE spectral synthesis code (V. Tsymbal, T. Ryabchikova & T. Sitnova 2019) alongside a grid of stellar atmosphere models precomputed with the LLMODELS code (D. Shulyak et al. 2004). The synthesis process was facilitated using the IDL-based interface BINMAG6 (O. Kochukhov 2018). All calculations were performed under the assumption of local thermodynamic equilibrium (LTE). Atomic data and spectral line parameters were adopted from the third release of the Vienna Atomic Line Database (VALD3; T. Ryabchikova et al. 2015).

For each chemical species, the final abundance was calculated as the mean of the values obtained from all relevant spectral segments. The standard error of the mean was taken as the uncertainty when an element was detected in multiple segments. Table 11 lists the measured abundances along with the number of contributing segments (in parentheses). The overall abundance patterns of the analysed stars, referenced to the solar composition of M. Asplund et al. (2009), are illustrated in Fig. 5.

HD 73135 exhibits marked chemical peculiarities characteristic of an Am star, with strong overabundances of Sr and Ba ($[\mathrm{X/H}] \gtrsim +1$) together with clear underabundances of Ca and Sc. This combination of heavy-element enhancement and Ca–Sc depletion is the defining abundance signature of the CP object in our sample.

BD $+19^\circ$ 2045 does not exhibit the characteristic abundance pattern of an Am star. In contrast to HD 73135, it shows neither the coupled Ca–Sc depletion nor the pronounced enhancement of iron-peak and heavy elements that typify metallic-line A stars. Its abundance distribution is therefore consistent with a chemically normal late-F star, within the measurement uncertainties and the expected element-to-element scatter. We consequently classify BD $+19^\circ$ 2045 as chemically non-peculiar.

The two K-type stars, BD $+19^\circ$ 2046 and TYC 1395−855−1, are discussed only in terms of their general photospheric composition. BD $+19^\circ$ 2046 is approximately solar in metallicity, with $\Delta \log N(\mathrm{Fe}) \simeq -0.08$ dex, and most elements lying within a few tenths of a dex of the solar reference. Moderate deviations are seen for some species, including enhancements of Ti, V, Mn, Cu, and Ba, and subsolar Si, Zn, and Ga. TYC 1395−855−1 is also close to solar in iron, with $\Delta \log N(\mathrm{Fe}) \simeq +0.04$ dex, but shows mild enhancements in several light and iron-peak elements, particularly Na, Mg, Al, Ti, V, Mn, and Cu, while Si and Sr are subsolar. These element-to-element variations are treated as part of the general spectroscopic characterization of the stars.

The pronounced heavy-element enhancements together with Ca–Sc depletion in HD 73135 are consistent with radiative diffusion and gravitational settling in a stable stellar atmosphere. By contrast, the other three stars show no comparable, internally consistent Am-type pattern. For CP stars, a single scaled-solar metallicity parameter [M/H] (as used in global spectral fitting) should not be interpreted as a true bulk metallicity; the chemically meaningful description is instead provided by [Fe/H] (Table 10) and the element-by-element abundances (Table 11).

5.7.1 NLTE effects on derived abundances

A brief assessment of NLTE effects indicates that HD 73135 [$T_{\mathrm{eff}} = 7210 \pm 110$ K, $\log g = 3.95 \pm 0.08$ (dex)] requires the largest abundance adjustments up to $\sim$0.2 dex for the O I 777 nm triplet, Na I D lines, and Fe I, while its Sr II and Ba II resonance lines incur corrections of $\lesssim$0.1 dex (S. M. Andrievsky et al. 2009; K. Lind et al. 2011; L. Mashonkina et al. 2011; T. M. Sitnova, L. I. Mashonkina & T. A. Ryabchikova 2013). For BD $+19^\circ$ 2045 ($T_{\mathrm{eff}} = 6440 \pm 180$ K, $\log g = 4.05 \pm 0.13$ (dex)), offsets shrink to $\sim$0.05–0.08 dex (Na, Mg) and $\leq$0.05 dex for Fe I and heavy-element lines (M. Bergemann et al. 2012). The cooler stars BD $+19^\circ$ 2046 and TYC 1395-855-1 exhibit NLTE corrections $\lesssim$0.05 dex for all species (L. Mashonkina, A. J. Korn & N. Przybilla 2007). Thus, while LTE abundances suffice to better than 0.05 dex for the cooler targets, line-by-line NLTE corrections are advisable for HD 73135 when pursuing precision below this threshold.

With these methodological clarifications, the parameters in Table 10 and the abundances in Table 11 can be considered internally consistent and sufficiently accurate for the evolutionary analysis in Section 6.

6 FUNDAMENTAL PARAMETERS AND EVOLUTIONARY PHASES

6.1 Masses, radii, and ages from forward modelling

We adopt the MIST stellar evolutionary tracks (J. Choi et al. 2016; A. Dotter 2016) which are computed using a one-dimensional (1D) stellar evolution code MESA (Modules for Experiments in Stellar Astrophysics; B. Paxton et al. 2011, 2013, 2015, 2018, 2019; A. S. Jermyn et al. 2023). We used MIST tracks for three reasons: (i) MIST is computed with a single version of the MESA code, ensuring that low- and intermediate-mass tracks share identical opacities, nuclear rates, overshoot and diffusion prescriptions, important when comparing an Am star, an F dwarf, and K-subgiants within one sample. (ii) The grid spans $-2.0 \leq [\mathrm{Fe/H}] \leq +0.5$ dex in 0.25-dex steps, fully bracketing our spectroscopic metallicities. (iii) Fine timesteps ($\Delta \log t = 0.02$) minimize interpolation artefacts in the subgiant phase, critical for modelling BD $+19^\circ$ 2046 and TYC 1395-855-1.

For each star, we take the spectroscopic T_{eff}, $\log(L_\star/L_\odot)$, $\log g$, and [Fe/H] computed as described in Section 5, and compare them with their corresponding model quantities $T_{\mathrm{eff,mod}}$, $\log L_{\mathrm{mod}}$,

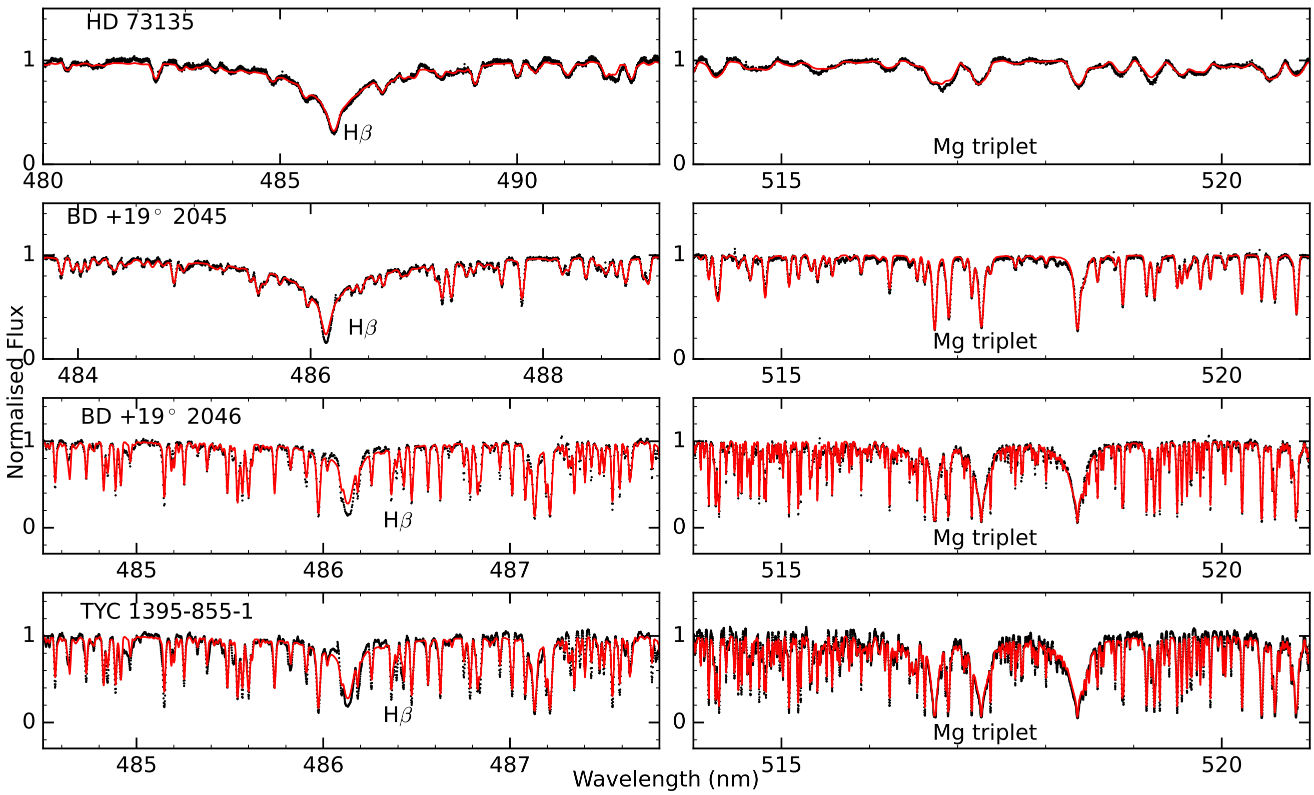

Figure 4. The Hβ (left) and Mg I triplet (right) regions of the spectra for the target stars. In each panel, the observed spectrum (black) is overplotted with the best-fitting synthetic spectrum (red). All spectra have been shifted to the stellar rest frame using the measured radial velocities (Table 10), so the Doppler shifts are removed by construction. For the K-type stars, the poorer Hβ fits are expected because the Balmer lines are intrinsically weaker and more affected by metal-line blending and continuum-normalization uncertainties in this regime. We therefore do not use the Balmer profiles of BD +19° 2046 and TYC 1395−855−1 as quantitative constraints on the atmospheric parameters.

$\log g_{\rm mod}$, and [Fe/H]$_{\rm mod}$ using a χ^2 expressed as

$$\chi^2 = \sum_i \frac{(\mathrm{obs}_i - \mathrm{mod}_i)^2}{\sigma_i^2}, \quad (3)$$

where $i \in \{T_{\rm eff}, \log(L_\star/L_\odot), \log g, [\mathrm{Fe/H}]\}$.

We note that stellar luminosities, expressed as $\log(L_\star/L_\odot)$, were determined using *Gaia* Data Release 3 (*Gaia* DR3) parallaxes (including zero-point corrections; C. Babusiaux et al. 2023) and apparent magnitudes, with interstellar extinction A_V as described in Section 5.2. Bolometric corrections were adopted from P. J. Flower (1996), updated by G. Torres (2010). The resulting $\log(L_\star/L_\odot)$ values for all programme stars are given in Table 12.

For each MIST grid point, we compute a relative posterior weight:

$$w \propto e^{-\chi^2/2}\,\Delta t, \quad (4)$$

where $e^{-\chi^2/2}$ is the likelihood term and Δt is the local timestep spacing in linear age, included to account for the evolutionary dwell time. These weights were calculated in our forward-modelling routine, normalized over the grid, and then used to construct the weighted distributions of mass, radius, and age. The 16th, 50th, and 84th percentiles of these distributions provide the median estimates and associated 68 per cent credible intervals; these results are presented in Table 12.

To assess the evolutionary status, we plot our target stars on the Hertzsprung–Russell diagram (Fig. 6), alongside evolutionary tracks (1.2–2.4 $M_\odot$ in 0.2 $M_\odot$ steps). HD 73135 and BD +19 2045 lie near the terminal-age main sequence, BD +19 2046 is located at the base of the red giant branch, and TYC 1395-855-1 is ascending the red giant branch. HD 73135 falls within the δ Scuti instability strip (S. J. Murphy et al. 2019), consistent with its classification as a potential pulsator.

7 CONCLUSIONS

We have presented a combined analysis of ground-based, *K2*, and *TESS* photometry together with high-resolution HERMES spectroscopy for four bright stars (HD 73135, BD +19° 2045, BD +19° 2046, and TYC 1395-855-1) originally monitored, but not fully characterized, under the Nainital–Cape Survey. We aimed to (i) search for and characterize low-amplitude variability and assess the consistency of multiple photometric diagnostics, (ii) determine spectral classifications and atmospheric parameters and identify chemical peculiarities where present, and (iii) infer fundamental parameters, including mass, radius, and age, using MIST evolutionary models.

The ground-based Johnson B, V photometry does not reveal any significant intrinsic periodicity, and the strongest frequency peaks are consistent with diurnal window-function and extinction-related artefacts. In contrast, the space-based photometry reveals clear low-amplitude variability, but with different behaviours in the four stars. HD 73135 shows a persistent ∼1.5 d signal in *K2*, which is most plausibly interpreted as

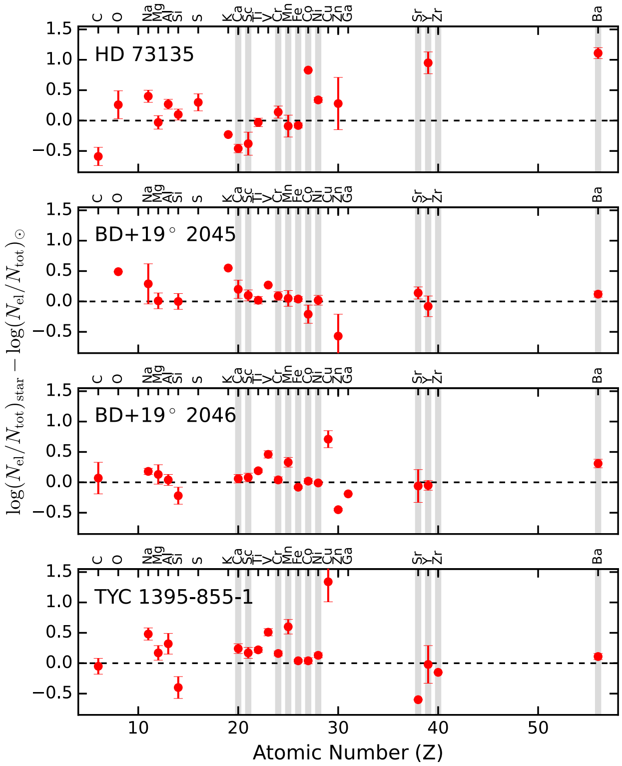

Figure 5. The abundances of chemical elements of the target stars as a function of atomic number relative to the solar values by M. Asplund et al. (2009). The grey vertical background bars highlight the light elements (Ca and Sc) and heavy elements (Cr, Mn, Fe, Co, Ni, Sr, Y, Zr, and Ba) relevant for Am star classification.

Table 12. Fundamental parameters for the programme stars derived from MIST. Uncertainties denote the 16th–84th percentile range of the posterior.

Star	$\log(L_\star/L_\odot)$	M (M$_\odot$)	R (R$_\odot$)	Age (Gyr)
HD 73135	1.16±0.05	$1.76^{+0.04}_{-0.05}$	$2.40^{+0.15}_{-0.15}$	$1.12^{+0.14}_{-0.00}$
BD +19° 2045	0.75±0.18	$1.32^{+0.09}_{-0.07}$	$1.91^{+0.23}_{-0.21}$	$3.16^{+0.82}_{-0.65}$
BD +19° 2046	1.48±0.06	$2.25^{+0.10}_{-0.09}$	$6.33^{+0.59}_{-0.51}$	$0.79^{+0.10}_{-0.09}$
TYC 1395−855−1	1.16±0.06	$1.38^{+0.31}_{-0.25}$	$5.33^{+0.42}_{-0.41}$	$3.55^{+3.53}_{-1.77}$

rotational modulation, although an ellipsoidal-binary interpretation cannot yet be excluded without time-series radial velocities. BD +19° 2045 shows a stable pattern of low-frequency variability consistent with a candidate γ Doradus pulsator. BD +19° 2046 and TYC 1395-855-1 are non-variable or only marginally variable in *K2*, but both show coherent low-frequency modulation in *TESS*, which we conservatively classify as variability of uncertain origin.

The spectroscopic analysis identifies HD 73135 as the only CP object in the sample, with an Am-star abundance pattern, while BD +19° 2045 is a chemically normal F8 V star and BD +19° 2046 and TYC 1395-855-1 are chemically non-peculiar K-type subgiants. Forward modelling places HD 73135 and BD +19° 2045 near the main sequence, whereas the two K stars are at more evolved subgiant stages.

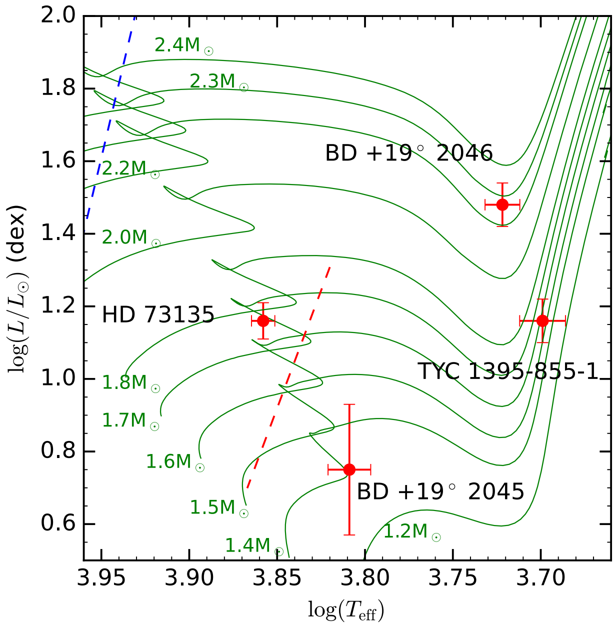

Figure 6. Hertzsprung–Russell diagram showing the positions of the sample stars. Solid green lines represent MIST evolutionary tracks for masses between 1.2 M$_\odot$ and 2.4 M$_\odot$. Blue and red dashed lines mark the empirical boundaries of the δ Scuti instability strip, as defined by S. J. Murphy et al. (2019).

The combination of time-series photometric observations with longer-baseline multi-epoch spectroscopy will be essential for refining the variability classifications and testing the physical origin of the signals in all studied stars. The upcoming space mission, *PLATO* (H. Rauer et al. 2025), will also provide valuable insights for improving the photometric characterization of BD +19° 2046 and TYC 1395-855-1.

ACKNOWLEDGEMENTS

We acknowledge funding through the Max Planck – Humboldt Research Unit, a partnership between the Max Planck Institute for Solar System Research (MPS) and Kyambogo University (KyU). BN also acknowledges additional funding through the Max Planck Partnership Group – SEISMIC project, a collaboration between the Max Planck Institute for Astrophysics (MPA), Germany, and Kyambogo University (KyU), Uganda. OT and EJ thank the International Science Programme (ISP) of Uppsala University for financial support. Part of work presented here is supported by the Belgo-Indian Network for Astronomy & Astrophysics (BINA), approved by the International Division, Department of Science and Technology (DST, Govt. of India; DST/INT/Belg/P-02) and the Belgian Federal Science Policy Office (BELSPO, Govt. of Belgium; BL/33/IN12). SJ, SCG, and OT acknowledge the financial support received from the BRICS grant under the project DST/IC/BRICS/2023/5. BN and RS acknowledge funding from the UNESCO-TWAS programme, 'Seed Grant for African Principal Investigators' financed by the German Ministry of Education and Research (BMBF). We acknowledge the use of SIMBAD and NASA's ADS. OV acknowledges funding from the Research Foundation Flanders (FWO), Grant No. 1173025N. This paper includes data collected by the *Kepler* mission available at *Mikulski Archive for Space*

Telescopes (*MAST*) operated by NASA. We thank the anonymous reviewers for a careful reading of the manuscript and for many insightful comments and suggestions that have improved the paper.

DATA AVAILABILITY

The high-resolution spectroscopic data used in this article will be shared upon reasonable request. The *K2* and *TESS* light curves for the target stars are publicly available on the *MAST* archive.[4]

SUPPLEMENTARY MATERIAL

Supplementary material are available at *MNRAS* online.

supplementary_material_mnras.pdf

Please note: Oxford University Press is not responsible for the content or functionality of any supplementary materials supplied by the authors. Any queries (other than missing material) should be directed to the corresponding author for the article.

REFERENCES

Aerts C., Christensen-Dalsgaard J., Kurtz D. W., 2010, Asteroseismology. Springer, Dordrecht
Aigrain S., Hodgkin S. T., Irwin M. J., Lewis J. R., Roberts S. J., 2015, MNRAS, 447, 2880
Aigrain S., Parviainen H., Pope B. J. S., 2016, MNRAS, 459, 2408
Andrievsky S. M., Spite M., Korotin S. A., Spite F., François P., Bonifacio P., Cayrel R., Hill V., 2009, A&A, 494, 1083
Ashoka B. N. et al., 2000, BASI, 28, 251
Asplund M., Grevesse N., Sauval A. J., Scott P., 2009, ARA&A, 47, 481
Astropy Collaboration, 2013, A&A, 558, A33
Astropy Collaboration, 2018, AJ, 156, 123
Astropy Collaboration, 2022, ApJ, 935, 167
Babusiaux C. et al., 2023, A&A, 674, A32
Bayo A., Rodrigo C., Barrado Y Navascués D., Solano E., Gutiérrez R., Morales-Calderón M., Allard F., 2008, A&A, 492, 277
Bergemann M., Lind K., Collet R., Magic Z., Asplund M., 2012, MNRAS, 427, 27
Bidelman W. P., 1956, PASP, 68, 318
Blanco-Cuaresma S., 2019, MNRAS, 486, 2075
Blanco-Cuaresma S., Soubiran C., Jofré P., Heiter U., 2014, A&A, 569, A111
Borucki W. J. et al., 2010, Science, 327, 977
Breger M. et al., 1993, A&A, 271, 482
Breger M. et al., 1999, A&A, 349, 225
Burdanov A. Y., Krushinsky V. V., Popov A. A., 2014, Astrophys. Bull., 69, 368
Cannon A. J., Pickering E. C., 1993, VizieR Online Data Catalog, p. III/135A
Cardelli J. A., Clayton G. C., Mathis J. S., 1989, ApJ, 345, 245
Castelli F., Kurucz R. L., 2003, in Piskunov N., Weiss W. W., Gray D. F., eds, IAU Symp. Vol. 210. Modelling of Stellar Atmospheres. p. A20
Catanzaro G., Frasca A., Giarrusso M., Ripepi V., Leone F., Tognelli E., Munari M., Scuderi S., 2018, MNRAS, 477, 2020
Catanzaro G., Busà I., Gangi M., Giarrusso M., Leone F., Munari M., 2019, MNRAS, 484, 2530
Ceillier T. et al., 2016, MNRAS, 456, 119
Ceillier T. et al., 2017, A&A, 605, A111
Choi J., Dotter A., Conroy C., Cantiello M., Paxton B., Johnson B. D., 2016, ApJ, 823, 102
Cowley A. P., Cowley C. R., 1965, PASP, 77, 184

[4]https://mast.stsci.edu/portal/Mashup/Clients/Mast/Portal.html.

Cutri R. M. et al., 2003, VizieR Online Data Catalog, p. II/246
Dileep A. et al., 2025, MNRAS, 542, 747
Dotter A., 2016, ApJS, 222, 8
Flower P. J., 1996, ApJ, 469, 355
Frémat Y., Neiner C., Hubert A. M., Floquet M., Zorec J., Janot-Pacheco E., Renan de Medeiros J., 2006, A&A, 451, 1053
Gaia Collaboration, 2021, A&A, 649, A1
González Hernández J. I., Bonifacio P., 2009, A&A, 497, 497
Gray D. F., 2005, The Observation and Analysis of Stellar Photospheres, Cambridge Univ. Press, UK
Gray R. O., Corbally J.C., 2009, Stellar Spectral Classification, Princeton Univ. Press
Gray R. O., Corbally C. J., 2014, AJ, 147, 80
Gray R. O., Corbally C. J., Garrison R. F., McFadden M. T., Robinson P. E., 2003, AJ, 126, 2048
Green G. M., 2018, JOSS, 3, 695
Green G. M., Schlafly E., Zucker C., Speagle J. S., Finkbeiner D., 2019, ApJ, 887, 93
Hauck B., Mermilliod M., 1998, A&AS, 129, 431
von Hippel T., Storrie-Lombardi L. J., Storrie-Lombardi M. C., Irwin M. J., 1994, MNRAS, 269, 97
Høg E. et al., 2000, A&A, 355, L27
Howell S. B. et al., 2014, PASP, 126, 398
Huber D. et al., 2014, ApJS, 211, 2
Jermyn A. S. et al., 2023, ApJS, 265, 15
Joshi S. et al., 2003, MNRAS, 344, 431
Joshi S., Mary D. L., Martinez P., Kurtz D. W., Girish V., Seetha S., Sagar R., Ashoka B. N., 2006, A&A, 455, 303
Joshi S., Mary D. L., Chakradhari N. K., Tiwari S. K., Billaud C., 2009, A&A, 507, 1763
Joshi S. et al., 2016, A&A, 590, A116
Joshi S., Semenko E., Moiseeva A., Sharma K., Joshi Y. C., Sachkov M., Singh H. P., Yerra B. K., 2017, MNRAS, 467, 633
Joshi S. et al., 2022, MNRAS, 510, 5854
Joshi S. et al., 2025, MNRAS, 543, 640
Kallinger T. et al., 2014, A&A, 570, A41
Kochukhov O., 2018, Astrophysics Source Code Library, record ascl:1805.015
LaSala J., 1994, in Corbally C. J., Gray R. O., Garrison R. F. eds, ASP Conf. Ser. Vol. 60, The MK Process at 50 Years: A Powerful Tool for Astrophysical Insight. Astron. Soc. Pac., San Francisco, p. 312
Lightkurve Collaboration, 2018, Astrophysics Source Code Library, record ascl:1812.013
Lind K., Asplund M., Barklem P. S., Belyaev A. K., 2011, A&A, 528, A103
Lipunov V. et al., 2010, Adv. Astron., 2010, 349171
Liu Y., San Liang X., Weisberg R. H., 2007, J. Atmos. Ocean. Technol., 24, 2093
Lomb N. R., 1976, Ap&SS, 39, 447
Martinez P. et al., 2001, A&A, 371, 1048
Mashonkina L., Korn A. J., Przybilla N., 2007, A&A, 461, 261
Mashonkina L., Gehren T., Shi J.-R., Korn A. J., Grupp F., 2011, A&A, 528, A87
Michaud G., Alecian G., Richer J., 2015, Astronomy and Astrophysics Library. Atomic Diffusion in Stars. Springer, Cham
Montgomery M. H., Odonoghue D., 1999, Delta Scuti Star Newslett., 13, 28
Moon T. T., Dworetsky M. M., 1985, MNRAS, 217, 305
Morel T., Butler K., 2006, A&A, 457, 651
Morgan W. W., Keenan P. C., Kellman E., 1943, An Atlas of Stellar Spectra, with an Outline of Spectral Classification. Univ. Chicago Press
Murphy S. J., Hey D., Van Reeth T., Bedding T. R., 2019, MNRAS, 485, 2380
Napiwotzki R., Schoenberner D., Wenske V., 1993, A&A, 268, 653
Paxton B., Bildsten L., Dotter A., Herwig F., Lesaffre P., Timmes F., 2011, ApJS, 192, 3
Paxton B. et al., 2013, ApJS, 208, 4
Paxton B. et al., 2015, ApJS, 220, 15
Paxton B. et al., 2018, ApJS, 234, 34

Paxton B. et al., 2019, ApJS, 243, 10
Press W. H., Teukolsky S. A., Vetterling W. T., Flannery B. P., 2007, Numerical Recipes: The Art of Scientific Computing, 3rd ed. Cambridge Univ. Press, Cambridge
Preston G. W., 1974, ARA&A, 12, 257
Raskin G. et al., 2011, A&A, 526, A69
Rauer H. et al., 2025, Exp. Astron., 59, 26
Ricker G., 2021, in 43rd COSPAR Scientific Assembly. p. 499
Ricker G. R. et al., 2015, J. Astron. Telesc. Instrum. Syst., 1, 014003
Rieke G. H., Lebofsky M. J., 1985, ApJ, 288, 618
Roederer I. U., Kirby E. N., 2014, MNRAS, 440, 2665
Roeser S., Bastian U., 1988, A&AS, 74, 449
Royer P. et al., 2024, A&A, 681, A107
Ryabchikova T., Piskunov N., Kurucz R. L., Stempels H. C., Heiter U., Pakhomov Y., Barklem P. S., 2015, Phys. Scr., 90, 054005
Scargle J. D., 1982, ApJ, 263, 835
Shulyak D., Tsymbal V., Ryabchikova T., Stütz C., Weiss W. W., 2004, A&A, 428, 993
Sitnova T. M., Mashonkina L. I., Ryabchikova T. A., 2013, Astron. Lett., 39, 126
Smalley B., 2005, Mem. Soc. Astron. Ital. Suppl., 8, 130
Smalley B. et al., 2017, MNRAS, 465, 2662
Stetson P. B., 1987, PASP, 99, 191
Tonry J., Davis M., 1979, AJ, 84, 1511
Torrence C., Compo G. P., 1998, BAMS, 79, 61
Torres G., 2010, AJ, 140, 1158
Trust O., Jurua E., De Cat P., Joshi S., Lampens P., 2021, MNRAS, 504, 5528
Tsymbal V., Ryabchikova T., Sitnova T., 2019, in Kudryavtsev D. O., Romanyuk I. I., Yakunin I. A., eds, ASP Conf. Ser. Vol. 518, Physics of Magnetic Stars. Astron. Soc. Pac., San Francisco, p. 247
Turcotte S., Richer J., Michaud G., Christensen-Dalsgaard J., 2000, A&A, 360, 603
Van Cleve J. E., Caldwell D. A., 2016, in Haas M. R., Howell S. B., eds, Kepler Instrument Handbook, Kepler Science Document KSCI-19033-002. p. 1

This paper has been typeset from a TEX/LATEX file prepared by the author.